Wetting of prototypical one- and two-dimensional systems: Thermodynamics and density functional theory

Petr Yatsyshin, Nikos Savva, and Serafim Kalliadasis

Citation: The Journal of Chemical Physics **142**, 034708 (2015); doi: 10.1063/1.4905605
View online: http://dx.doi.org/10.1063/1.4905605
View Table of Contents: http://scitation.aip.org/content/aip/journal/jcp/142/3?ver=pdfcov
Published by the AIP Publishing

Wetting of prototypical one- and two-dimensional systems: Thermodynamics and density functional theory

Petr Yatsyshin,[1] Nikos Savva,[1,2] and Serafim Kalliadasis[1]
[1]*Department of Chemical Engineering, Imperial College London, London SW7 2AZ, United Kingdom*
[2]*School of Mathematics, Cardiff University, Cardiff CF24 4AG, United Kingdom*

(Received 24 October 2014; accepted 24 December 2014; published online 21 January 2015)

Consider a two-dimensional capped capillary pore formed by capping two parallel planar walls with a third wall orthogonal to the two planar walls. This system reduces to a slit pore sufficiently far from the capping wall and to a single planar wall when the side walls are far apart. Not surprisingly, wetting of capped capillaries is related to wetting of slit pores and planar walls. For example, the wetting temperature of the capped capillary provides the boundary between first-order and continuous transitions to condensation. We present a numerical investigation of adsorption in capped capillaries of mesoscopic widths based on density functional theory. The fluid-fluid and fluid-substrate interactions are given by the pairwise Lennard-Jones potential. We also perform a parametric study of wetting in capped capillaries by a liquid phase by varying the applied chemical potential, temperature, and pore width. This allows us to construct surface phase diagrams and investigate the complicated interplay of wetting mechanisms specific to each system, in particular, the dependence of capillary wetting temperature on the pore width. © *2015 AIP Publishing LLC.* [http://dx.doi.org/10.1063/1.4905605]

I. INTRODUCTION

Studies of nano-confined fluids are motivated by fundamental as well as applied interest. From a theoretical point of view, a fluid confined inside a small pore is a statistical-mechanical system with a rich phase behavior since the parameters of the fluid-substrate potential and the characteristic dimensions of the pore act as thermodynamic degrees of freedom. In applications, enhancing our understanding of adsorption in small pores is essential in new and rapidly developing branches of engineering and science such as micro- and nano-fluidics,[1–5] biomimetics,[6,7] colloidal science,[8–10] and the design and operation of lab-on-a chip devices.[11,12] Investigations of wetting in prototypical nano-sized pores also provide a foundation for understanding adsorption on patterned substrates and the phenomenon of superhydrophobicity and superspreading.[13,14]

In this study, we consider three prototypical systems, a planar wall, a slit pore, and a capped capillary in contact with undersaturated vapor of a fluid with long-range intermolecular fluid-fluid and fluid-substrate interactions. The three systems are sketched in the top panels (a), (b), and (c) of Fig. 1. The bottom panels of Fig. 1 show the respective wetting phase diagrams. It is convenient to define the (negative) deviation chemical potential $\Delta\mu = \mu - \mu_{\text{sat}}$, where $\mu_{\text{sat}}(T)$ is the saturation chemical potential at the given temperature T. We will use $\Delta\mu$ instead of μ when plotting the isotherms and wetting phase diagrams.

Consider first a planar wall, Fig. 1(a). For $\Delta\mu = 0$ and $T = T_{\text{w}}$ (wetting temperature), the fluid in contact with the wall undergoes a first-order wetting transition.[15–18] For $\Delta\mu < 0$, there is a line of first-order prewetting transitions (the coexistence of thin and thick adsorbed liquid films is often referred to as prewetting), $\Delta\mu_{\text{pw}}(T)$, which approaches saturation tangentially at T_{w}. If saturation is approached from below at $T > T_{\text{w}}$, the transition to wetting is continuous (complete wetting transition). At saturation, the macroscopic contact angle Θ of a sessile liquid drop sitting on a planar wall is given by the Young equation

$$\sigma_{\text{wv}} = \sigma_{\text{wl}} + \sigma_{\text{lv}} \cos\Theta, \tag{1}$$

where σ_{wv}, σ_{wl}, and σ_{lv} are wall-vapor, wall-liquid, and liquid-vapor surface tensions, respectively. The wall wetting temperature satisfies the condition

$$\Theta(T_{\text{w}}) = 0. \tag{2}$$

We now turn to a slit pore formed by two parallel walls with H the separation distance, Figure 1(b). When $\mu_{\text{c}} < \mu_{\text{sat}}$, the fluid in the pore undergoes a first-order condensation transition. During condensation vapor coexists with liquid, which is metastable in the bulk, hereinafter referred to as capillary liquid. The value of μ_{c} at low T is often approximated

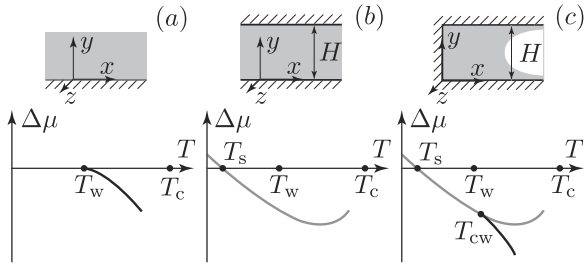

FIG. 1. The geometries under consideration (top) and their respective wetting phase diagrams (bottom) for a planar wall (a), a slit pore (b), and a capped capillary (c). Top of each panel: hatched and gray-shaded areas represent the substrate and the adsorbate, respectively. Bottom of each panel: black and gray curves correspond to the prewetting [referred to as $\Delta\mu_{\text{pw}}(T)$ for (a) and $\Delta\mu_{\text{cpw}}(T)$ for (c)] and condensation [$\Delta\mu_{\text{c}}(T)$] transition curves, respectively.

using the phenomenological Kelvin equation[15,18]

$$\mu_c = \mu_{sat} - \frac{2\sigma_{lv}\cos\Theta}{H\Delta\rho}, \tag{3}$$

where $\Delta\rho = \rho_{liq} - \rho_{vap}$ is the difference between bulk liquid and vapor number densities at $\Delta\mu = 0$. According to Eq. (3), the transition curve $\Delta\mu_c(T)$ crosses saturation at T_s, where $\Theta(T_s) = \pi/2$, and has a minimum near T_w.[18]

Finally, we turn to the capped capillary, Figure 1(c). This system has been studied a lot less than a planar wall and a slit pore. Far from the capping wall, as $x \to \infty$, the capped capillary reduces to its associated slit pore, so the fluid should undergo condensation at μ_c given by Eq. (3). However, the order of the transition can be continuous, as was found by Parry *et al.*[19] A later density functional theory (DFT) study by Yatsyshin *et al.*[20] has revealed the existence of the capillary wetting temperature, T_{cw}, which separates first-order and continuous condensation at μ_c. For $T \le T_{cw}$, condensation is first-order and for $T > T_{cw}$, it is continuous. When $T > T_{cw}$ and $\mu < \mu_c$ (but not too far from μ_c), the cumulative action of the substrate behind the capping wall may serve to nucleate a slab of capillary liquid, which is then separated from the vapor by a circular-arc meniscus. The continuous unbinding of the meniscus as $\mu \to \mu_c^-$ marks the onset of condensation above T_{cw}.

The DFT calculations performed by Yatsyshin *et al.*,[20] and independently by Malijevský[21] for a similar system, also suggested that condensation above T_{cw} may be preceded by the capillary prewetting transition and a resulting hysteresis in the growth of the capillary liquid slab. During capillary prewetting, vapour and a slab of capillary liquid of mesoscopic height adsorbed on the capping wall coexist. The locus of the transitions, $\Delta\mu_{cpw}(T)$, is sketched in the bottom panel of Fig. 1. The curve $\Delta\mu_{cpw}(T)$ approaches the condensation curve $\Delta\mu_c(T)$ tangentially at T_{cw}. Such phenomenology of capped capillaries is clearly analogous to wetting of planar walls. A recent study by Rascon *et al.*[22] has explored the effect of the wetting properties of the capping wall on the order of condensation at T_{cw}. Using an effective Hamiltonian approach, the authors have revealed that T_{cw} is related to the Young contact angle of the capping wall considered on its own.

In what follows, we consider the three systems from Fig. 1 using DFT.[23] All intermolecular interactions are modelled by the Lennard-Jones (LJ) pairwise potential

$$\varphi^{6-12}_{\varepsilon_0,\sigma_0}(r) = 4\varepsilon_0\left[-\left(\frac{\sigma_0}{r}\right)^6 + \left(\frac{\sigma_0}{r}\right)^{12}\right], \tag{4}$$

where ε_0 and σ_0 are measures of the strength and range of the potential, respectively. We work sufficiently below the bulk critical temperature, T_c, where the classical DFT approach is applicable, neglecting also the density fluctuations along the z-axis. At the same time, T is taken above the bulk triple point, where there is no freezing or layering in the fluid.

Our goal is to understand the connections of wetting in the capped capillary to wetting on a wall and in a slit pore, which provide two different limiting cases ($H \to \infty$ and $x \to \infty$, respectively). For example, the adsorption of capillary liquid slab on the capping wall of the capillary and the adsorption of liquid film on an infinite planar wall are related phenomena.[22] What is then the effect of the pore width? To what extent can one consider the value of T_w to be an approximation to T_{cw}? How well does the Kelvin equation describe condensation in slit pores and capped capillaries at low temperatures? Only a detailed calculation using a microscopic approach, such as that provided by DFT, can address these and similar questions. Details of the DFT we use and the governing equations are given in Sec. II. Calculation results are detailed in Sec. III, with a brief summary given in Sec. IV.

II. THEORETICAL FRAMEWORK

Treating the substrate as a spectator phase which gives rise to the external potential $V_{ext}(\mathbf{r})$, the fluid grand potential can be approximated as a functional of the spatially distributed one-body number density $\rho(\mathbf{r})$,[23,24]

$$\Omega[\rho(\mathbf{r})] = F_{in}[\rho(\mathbf{r})] + \int d\mathbf{r}\rho(\mathbf{r})(V_{ext}(\mathbf{r}) - \mu), \tag{5}$$

where $F_{in}[\rho]$ is the "intrinsic" free energy functional, which does not depend on $V_{ext}(\mathbf{r})$; integration is carried out over the volume V occupied by the fluid. At equilibrium, $\rho(\mathbf{r})$ minimises $\Omega[\rho(\mathbf{r})]$, which is then equal to the grand potential $\Omega(T,V,\mu)$. Taking the hard sphere fluid as a reference system and the LJ attractions as a perturbation, $F_{in}[\rho]$ can be approximated as

$$\begin{aligned} F_{in}[\rho(\mathbf{r})] = {} & k_BT\int d\mathbf{r}\rho(\mathbf{r})\left(\ln\lambda^3\rho(\mathbf{r}) - 1\right) \\ & + \int d\mathbf{r}\rho(\mathbf{r})\psi(\rho(\mathbf{r})) \\ & + \frac{1}{2}\int d\mathbf{r}\int d\mathbf{r}'\rho(\mathbf{r})\rho(\mathbf{r}')\varphi_{attr}(|\mathbf{r}-\mathbf{r}'|), \end{aligned} \tag{6}$$

where k_B is the Boltzmann constant, λ is the de Broglie wavelength, $\psi(\rho)$ is the configurational part of the hard sphere fluid free energy per particle, and $\varphi_{attr}(r)$ is the attractive potential. The first term in the right hand side of Eq. (6) corresponds to the ideal gas free energy, the second term accounts for the hard sphere repulsions at short distances, and the third term accounts for the LJ attractions. With the Carnahan-Starling equation of state for the hard sphere fluid,[25] the expression for $\psi(\rho)$ is given by

$$\psi(\rho) = k_BT\frac{\eta(4-3\eta)}{(1-\eta)^2}, \quad \eta = \pi\sigma^3\rho/6, \tag{7}$$

where σ is the hard sphere diameter. The attractive potential can be approximated with the Barker-Henderson perturbation theory[26]

$$\varphi_{attr}(r) = \begin{cases} 0, & r \le \sigma \\ \varphi^{6\text{-}12}_{\varepsilon,\sigma}, & r > \sigma \end{cases}, \tag{8}$$

where ε is the depth of the attractive potential well. In Eq. (8) we have neglected the weak temperature dependence of σ. When $\rho(\mathbf{r})$ is constant in one [Fig. 1(c)] or two [Figs. 1(a) and 1(b)] directions, the last term in Eq. (6) can be simplified by integrating $\varphi_{attr}(r)$ along the directions of constant density, see Appendix A.

The local density approximation for the repulsive contribution to $F_{in}[\rho]$ [second term in Eq. (6)] does not properly

account for the excluded volume correlations in the fluid. As a result, the fluid density profiles obtained do not possess an oscillatory near-wall structure. This can be captured with more refined treatments such as fundamental measure theory.[27,28] Nevertheless, the local treatment of intermolecular repulsions we adopt here is suitable for the purposes of the present study. This is because we investigate wetting by a liquid phase above the bulk triple point, where the fluid surface phase behavior is determined by the asymptote of the pairwise attractive potentials,[29] and the description of short-range intermolecular repulsions[30] offered by this treatment adequately captures the main features of the phenomenology we wish to discuss. Our treatment of attractions [last term in Eq. (6)] corresponds to the random phase approximation, which captures the asymptotic behavior of the fluid direct pair correlation function in the bulk.[31]

The intermolecular fluid-substrate interactions are governed at long distances by the pairwise LJ potential in Eq. (4) with the substrate-specific parameters, $\varepsilon_0 = \varepsilon_w$, $\sigma_0 = \sigma_w$. In general, at short distances, the intermolecular potentials are different from LJ.[32] Moreover, integrating the LJ potential over the substrate volume to obtain the cumulative fluid-substrate potential $V_{ext}(\mathbf{r})$ leads to a non-physical divergence of $V_{ext}(\mathbf{r})$ at contact with the fluid. To remove the divergence, we introduce a near-wall shift H_0 of the cumulative substrate potential. One can think of the substrate surface as being coated by a layer of foreign solid phase of width H_0, where the coating does not exert a long-range potential on the fluid, and thus does not affect the corresponding wetting behavior. The cumulative substrate potential in Eq. (5) is given by

$$V_{ext}(\mathbf{r}) = \rho_w \int d\mathbf{r}' \varphi^{6-12}_{\varepsilon_w,\sigma_w}(|\mathbf{r}-\mathbf{r}'|), \tag{9}$$

where ρ_w is the effective density of the LJ substrate, and the integration is carried out over the volume of the substrate excluding the coating. The potential of the planar wall [Fig. 1(a), the fluid has y-dependent density, $\rho(\mathbf{r}) \equiv \rho_{wall}(y)$, defined for $\mathbf{r} = (x,y,z)$ with $x,z \in (-\infty,+\infty)$ and $y \in [0,+\infty)$] is given by

$$V_{wall}(y) = 4\pi\rho_w\varepsilon_w\sigma_w^3\left(-\frac{1}{6}\left(\frac{\sigma_w}{H_0+y}\right)^3 + \frac{1}{45}\left(\frac{\sigma_w}{H_0+y}\right)^9\right). \tag{10}$$

The potential of the slit pore of width H [Fig. 1(b), the fluid has y-dependent density, $\rho(\mathbf{r}) \equiv \rho_{slit}(y)$, defined for $\mathbf{r} = (x,y,z)$ with $x,z \in (-\infty,+\infty)$ and $y \in [0,H]$] is given by

$$V_{slit}(y) = V_{wall}(y) + V_{wall}(H-y). \tag{11}$$

Finally, the potential of the capped capillary [Fig. 1(c), the fluid has x- and y-dependent density, $\rho(\mathbf{r}) \equiv \rho_{cpd}(x,y)$, defined for $\mathbf{r} = (x,y,z)$ with $x \in [0,+\infty)$, $y \in [0,H]$ and $z \in (-\infty,+\infty)$] is

$$V_{cpd}(x,y) = V_{slit}(y) + V_{cap}(x,y), \tag{12}$$

where the second term accounts for the contribution due to the capping wall

$$\begin{aligned} V_{cap}(x,y) &= \rho_w \int_{-\infty}^{-H_0} dx' \int_{-H_0}^{H+H_0} dy' \int_{-\infty}^{\infty} dz' \, \varphi^{6-12}_{\varepsilon_w,\sigma_w}(|\mathbf{r}-\mathbf{r}'|) \\ &= \frac{-3}{8}\frac{\rho_w\varepsilon_w\sigma_w^6\pi(H+2H_0)}{x^4} \\ &\quad + O\left(\frac{\rho_w\varepsilon_w\sigma_w^6 H_0(H+2H_0)}{x^5}\right), \end{aligned} \tag{13}$$

as $x \to \infty$.

The Euler–Lagrange equation for the minimization of $\Omega[\rho(\mathbf{r})]$ can be obtained by functional differentiation

$$\begin{aligned} &k_BT\ln\rho(\mathbf{r}) + \psi(\rho(\mathbf{r})) + \rho(\mathbf{r})\psi'_\rho(\rho(\mathbf{r})) \\ &\quad + \int d\mathbf{r}'\rho(\mathbf{r}')\varphi_{attr}(|\mathbf{r}-\mathbf{r}'|) + V_{ext}(\mathbf{r}) - \mu = 0, \end{aligned} \tag{14}$$

where ψ'_ρ is the derivative of $\psi(\rho)$ in Eq. (7) with respect to ρ. In the limit $V_{ext}(\mathbf{r}) \to 0$ and $\rho(\mathbf{r}) \to \rho = \text{const}$, Eqs. (14) and (5) are equivalent to the bulk equations of state

$$\mu = k_BT\ln\rho + \psi(\rho) + \rho\psi'_\rho(\rho) - \frac{32\pi}{9}\rho\sigma^3\varepsilon, \tag{15}$$

$$P = \rho k_BT\frac{1+\eta+\eta^2-\eta^3}{(1-\eta)^3} - \frac{16\pi}{9}\rho^2\sigma^3\varepsilon, \tag{16}$$

where P denotes pressure. At saturation, $\mu(\rho_{liq}) = \mu(\rho_{vap}) = \mu_{sat}$ and $P(\rho_{liq}) = P(\rho_{vap}) = P_{sat}$. At $T = T_c$, $\partial P/\partial\rho_c = \partial^2 P/\partial\rho_c^2 = 0$, where ρ_c is the bulk critical density. Given T and μ of the reservoir, we can obtain $\rho(\mathbf{r})$ by solving Eq. (14) and subsequently, the grand potential $\Omega(T,\mu)$ from Eq. (5).

A. Critical exponents

The effective binding potential[15] corresponding to the free energy functional in Eq. (5) can be obtained by substituting the "sharp-kink" parametrization of the density profile in terms of the local interface height.[18,33] For example, in the case, when a liquid film of height l is adsorbed on a planar wall, the density can be approximated by $\rho(\mathbf{r}) \equiv \rho_{sk}(y) = \rho_{liq}\Theta(l-y) + \rho_{vap}\Theta(y-l)$, where $\Theta(x)$ is the Heaviside step-function. Substituting into Eq. (5) with $V_{ext}(\mathbf{r}) = V_{wall}(y)$, one can identify the terms corresponding to the bulk energy contribution, surface tensions, and effective binding with potential $W(l)$. The latter is due to the substrate-fluid interactions, which decay with the distance to the wall[29]

$$\Omega(l)/A = -l\Delta\mu\Delta\rho + \sigma_{wl} + \sigma_{lv} + \Delta\rho W(l), \tag{17}$$

where A is the wall area and

$$\begin{aligned} W(l) &\equiv \int_l^\infty dz\left(\rho_{liq}\int_z^\infty dy\,\varphi_{attr}(y) - V_{wall}(z)\right) \\ &= A_H/l^2 + O\left(\varepsilon_w\rho_w\sigma_w^6 H_0/l^3\right), \end{aligned} \tag{18}$$

where it is assumed that l/σ_w is large, $\varphi_{attr}(y) = \int dxdz\varphi_{attr}(r)$, and A_H is the Hamaker constant[29]

$$A_H = \pi/3\left(\rho_w\varepsilon_w\sigma_w^6 - \rho_{liq}\varepsilon\sigma^6\right). \tag{19}$$

Note that A_H does not depend on H_0 from Eq. (10). Minimising $\Omega(l)$ with respect to l, we obtain

$$l = (2A_H)^{1/3}(-\Delta\mu)^{-1/3}, \tag{20}$$

which should hold near $\Delta\mu = 0$ for LJ intermolecular potentials.

Analogous considerations for the capped capillary have to take into account that a slab of capillary liquid of height l_s is adsorbed on the capping wall when $\mu < \mu_c$, due to the potential V_{cap}. Taking into account the asymptote of $V_{cap}(x,y)$ in Eq. (13), the capillary liquid slab adsorbed on the capping wall behaves as[19]

$$l_s \propto (\mu_c - \mu)^{-1/4}, \tag{21}$$

for μ approaching μ_c.

Note that $W(l)$ depends on the local film height. On the other hand, the non-local character of intermolecular interactions is properly expressed by the free energy functional in Eq. (6). In Sec. III, we contrast the DFT calculation with the predictions in Eqs. (20) and (21).

B. Phase transitions

To trace the various phase transitions, we fix T and vary μ to obtain a set of solutions $\{\rho(\mathbf{r})\}_\mu$ to Eq. (14) together with their corresponding grand potential isotherm $\Omega(\mu) = \Omega[\{\rho(\mathbf{r})\}_\mu]$, discarding the density profiles corresponding to non-concave branches of $\Omega(\mu)$. The remaining stable configurations may correspond to different fluid phases coexisting at some μ_0, where $\Omega(\mu_0)$ is non-analytic. A first-order transition corresponds to a discontinuity in $\partial\Omega(\mu)/\partial\mu$ at μ_0. The divergence of $\partial\Omega(\mu)/\partial\mu$, as $\mu \to \mu_0$, corresponds to a continuous transition at that point.

A first-order transition is expressed by the following system of equations for μ_0 and the coexisting density profiles $\rho_1(\mathbf{r})$ and $\rho_2(\mathbf{r})$:

$$\frac{\delta\Omega}{\delta\rho}\Big|_{\rho_1(\mathbf{r})} = \frac{\delta\Omega}{\delta\rho}\Big|_{\rho_2(\mathbf{r})} = 0, \tag{22a}$$

$$\Omega[\rho_1(\mathbf{r})] - \Omega[\rho_2(\mathbf{r})] = 0, \tag{22b}$$

where Eq. (22a) is equivalent to the Euler–Lagrange equation, Eq. (14) and Eq. (22b) expresses the condition that $\Omega(\mu)$ self-intersects at μ_0. Solving Eq. (22) for a range of values of T allows us to construct the phase diagrams sketched in Fig. 1. To compute wetting temperatures, one can make use of the Clausius–Clapeyron equation, which determines the slope of a phase coexistence curve $\mu_0(T)$,[34]

$$\frac{\partial\mu_0}{\partial T} = -\frac{S_1 - S_2}{N_1 - N_2}, \tag{23}$$

where N_1, S_1 and N_2, S_2 are the particle numbers and entropies of the coexisting fluid phases.

C. Surface excess quantities

For a given T, it is convenient to separate bulk and surface excess contributions to extensive thermodynamic variables. The bulk contribution to the grand free energy $(-PV)$ is the same for all the systems sketched in Fig. 1. In the cases of the wall and the slit pore, the excess grand free energy is given by[34]

$$\begin{aligned}\Omega^{ex}_{wall,\ slit}(\mu) &\equiv \Omega(\mu) + PV \\ &= \Omega\left[\rho_{wall,\ slit}(y)\right] - \Omega[\rho_b],\end{aligned} \tag{24}$$

where $\Omega[\rho(\mathbf{r})]$ is given in Eq. (5) and ρ_b is the bulk vapor density, which can be obtained as the root of Eq. (15). In the case of the wall, the fluid density $\rho_{wall}(y)$ is defined for $y \in [0,\infty)$, and for large y/σ_w, we have, to leading order, $\rho_{wall}(y) = \rho_b + \alpha/y^3 + \cdots$, where α is a dimensionless constant.[35] It then follows that $\Omega^{ex}_{wall}(\mu)$ is finite for wall wetting. In the case of the slit pore, the fluid density $\rho_{slit}(y)$ is defined between $y = 0$ and $y = H$, so $\Omega^{ex}_{slit}(\mu)$ is finite too. Finally, in the case of the capped capillary, the fluid density $\rho_{cpd}(x,y)$ is defined for $x \in [0,\infty)$ and $y \in [0,\infty)$. It follows from Eq. (13), that to leading order $\rho_{cpd}(x,y) = \rho_{slit}(y) + \kappa/x^4 + \cdots$, as $x \to \infty$, where κ has the dimensions of length. Therefore, if the expression in Eq. (24) is evaluated with $\rho_{cpd}(x,y)$, it would not give a finite quantity. A finite quantity is instead obtained by defining the excess grand free energy relative to the associated slit pore

$$\Omega^{ex}_{cpd}(\mu) = \Omega\left[\rho_{cpd}(x,y)\right] - \Omega\left[\rho_{slit}(y)\right]. \tag{25}$$

For the adsorption on the wall and in the slit pore, we have the usual expression[34]

$$\Gamma_{wall,\ slit} = \int dy\,(\rho_{wall,\ slit}(y) - \rho_b). \tag{26}$$

The Gibbs adsorption equation connects Γ and $\Omega^{ex}(\mu)$ at constant T through[34]

$$\Gamma_{wall,\ slit} = -1/A\left(\partial\Omega^{ex}_{wall,\ slit}/\partial\mu\right). \tag{27}$$

Following similar arguments, due to the asymptotic behavior of $\rho_{cpd}(x,y)$, a finite adsorption for wetting of the capped capillary can be defined as

$$\Gamma_{cpd} = \int dx \int dy\left(\rho_{cpd}(x,y) - \rho_{slit}(y)\right). \tag{28}$$

For a capillary with the macroscopic characteristic length scale R along the z-axis, the Gibbs adsorption equation takes the form

$$\Gamma_{cpd} = -1/R\left(\partial\Omega^{ex}_{cpd}/\partial\mu\right). \tag{29}$$

D. Numerical approach

Let us comment briefly on the numerical challenges associated with solving Eqs. (14) and (22) in one and two dimensions. Over the years, a number of numerical approaches have been proposed for solving DFT equations.[9,27,36–38] The crucial step in the numerical implementation is to accurately and efficiently compute the non-local integral terms corresponding to the fluid-fluid interactions, i.e., the fourth term in Eq. (14). Our recent studies for both local/differential equations[39,40] and non-local/integral equations[20,28,35] have highlighted the advantages of employing pseudospectral collocation methods.[41,42] For integral equations, we use the Clenshaw–Curtis quadrature to evaluate the non-local terms.[35,43] Regarding the spectral approach, it is noteworthy that it has an exponential convergence rate with the size

of the computational grid, while other methods used in the literature are typically based on the Simpson rule or fast Fourier transform and exhibit only algebraic convergence.[27,44] A faster convergence rate allows us to use significantly fewer grid points when discretising the computational domain, while retaining high accuracy in the computations. This is especially important in two-dimensional (2D) problems.

Pseudospectral methods for DFT are implemented by discretising $\rho(\mathbf{r})$ on a non-uniform grid of collocation points and constructing a globally interpolating function. All mathematical operations are performed on this global interpolant and have exponential accuracy. For the present study, the pseudospectral method developed for integral equations in Ref. 35 was extended to 2D problems by constructing the interpolant on a tensor product grid formed by conformally mapping a grid based on Chebyshev[42] points independently in each direction onto the physical domain of interest. The benefit of using conformal maps is that we can position the collocation points densely near the walls, where the density is expected to vary sharply, and at the same time, we can have grid points quite far from the adsorbing wall allowing us to capture the smooth decay of the density profile. This approach allows us to compute accurately the values of the critical exponents given in Eqs. (20) and (21). In practice, we positioned the last point at a distance of about $10^3\sigma$ from the adsorbing wall. For one-dimensional problems (1D, planar wall and slit pore), we used grid sizes of 130 points for the wall and up to 60 points for slit pores with various H. For 2D problems (capped capillary), we used 130 and up to 60 discretization points along the x- and y-directions, respectively. To obtain critical exponents and compute coexistence lines near the wetting temperatures, we sometimes increased the grid size to about 200 points along the direction of interface growth.

Discretizing the integral Eqs. (14) and (22) leads to systems of non-linear algebraic equations, which are solved using Newton's algorithm. A tolerance of 10^{-7} typically requires 2 or 3 iterations. The calculation time is significantly reduced by evaluating the non-local terms as a matrix-vector product and computing the matrix outside the Newton loop.

Figure 2 shows the results of a convergence test for the numerical solver of Eq. (14) for the capped capillary with $H = 30$. A density profile ρ_0 of a fluid configuration similar to the one shown in Fig. 8(d), with the center of the meniscus along the x-axis located at approximately 10 molecular diameters from the capping wall, was obtained on the reference grid with 162×80 points along the x- and y-axes, respectively. The same calculation was repeated on coarser meshes of size 32×16, 48×24, 72×36, and 108×54 obtaining ρ_N, where N is the total number of mesh points. In order to compare ρ_N with ρ_0, we interpolated both solutions on a truncated domain $[0,20]\times[0,30]$, which was discretized uniformly with $K = 2400$ points, using 2 points per molecular diameter along each dimension. The estimate of the average error is given as the mean of the Euclidean norm of the difference of the interpolated data, namely,

$$\mathcal{E} = \frac{1}{K}\sqrt{\sum_{i=0}^{K}[\rho_N^{(i)} - \rho_0^{(i)}]^2}, \tag{30}$$

where the superscript (i) is a label for points on the uniform grid.

Apart from the discretisation issues, selecting an initial guess for the Newton algorithm (or any other iterative scheme, e.g., Picard) to converge is a challenge. To overcome it, we employ a pseudo-arc-length continuation technique[35,45] which allows one to treat any parameter in the non-linear system of equations as an unknown and serves to optimize the selection of the initial guess. In Eq. (14), we choose μ as the continuation parameter and start our calculations at a rather low value of μ, where the fluid is dilute and a simple initial guess suffices to obtain the unique numerical solution. The continuation algorithm then proceeds to automatically vary the values of μ and provide an optimal initial guess for the Newton method to converge for every new value of μ. This allows us to obtain grand potential and adsorption isotherms in a systematic and efficient fashion. By applying the same method to Eqs. (22), we can trace the transitions with T as the continuation parameter and construct the phase diagrams of wetting.

All computations presented in Sec. III were performed on a standard desktop computer. In practice, in the cases of the wall and the slit pore, the calculation of a single density profile from Eq. (14) is fast, with the calculation of an isotherm (same equation, μ is treated as a parameter) taking several seconds, and the calculation of a phase diagram from Eqs. (22) with T treated as a parameter taking several minutes. For capped capillaries, the calculations of density profiles and of isotherms take about a minute and an hour, respectively. The calculation of a phase transition curve takes about three hours.

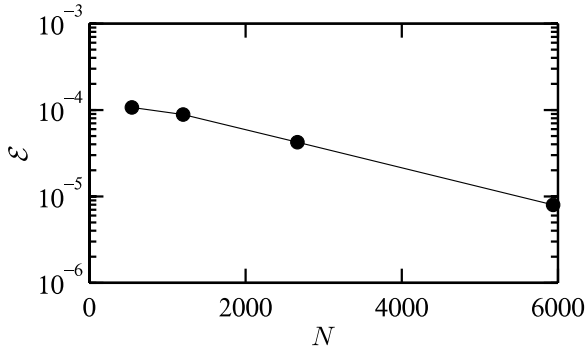

FIG. 2. Convergence of the numerical scheme with the number N of grid points.

III. NUMERICAL RESULTS AND DISCUSSION

We use the parameters σ and ε in Eqs. (7) and (8) as the units of length and energy. The bulk critical temperature is $T_c \approx 1.006$ (in units of ε/k_B). We set $\rho_w = 1$ in Eq. (9). The parameters ε_w, σ_w, and H_0 of the fluid-substrate potentials in Eqs. (10)–(12) were chosen to satisfy three criteria for the systems to exhibit the behaviour we wish to study: the planar wetting transition should be first-order, the planar prewetting on the side walls of the slit pores should be pre-empted by condensation, and lastly, there should be no remnant of wedge prefilling in the corners of capped capillaries.[20,46] The case, where prewetting films can form on the side walls of the

capped capillary and the case, where the wetting of 2D wedges is manifested by drops adsorbed in the corners of the capped capillary deserve a dedicated study and will not be considered here. Finally, we tried to get a substrate with $T_w \sim 0.9T_c$, in order for the interfaces to be smoother and not requiring too many grid points to be resolved. We thus fix the parameters of the substrate as $\varepsilon_w = 0.6$, $\sigma_w = 1.7$, $H_0 = 3.5$. The results we present should remain qualitatively unaltered for a broader class of long-range fluid-substrate potentials, which lead to first-order planar wetting.

A. Wall

Figure 3 shows planar prewetting at $T = 0.92$ and $\Delta\mu_{pw} = -0.1 \times 10^{-2}$. The adsorption isotherm $\Gamma_{wall}(\mu)$ is plotted in Fig. 3(a), with a dashed vertical line at $\Delta\mu_{pw}$ showing the equal-area construction. By setting the effective thickness of adsorbed film to be

$$l := \Gamma_{wall}/\Delta\rho, \tag{31}$$

we can connect with the phenomenology of prewetting discussed in Sec. I. The isotherm of excess grand potential per unit area is shown in Fig. 3(b). The Gibbs adsorption rule from Eq. (27) was used to verify the calculation. The intersection of the concave branches of $\Omega^{ex}_{wall}(\mu)$ suggests the presence of a first-order transition at $\Delta\mu_{pw}$ and hysteresis. The density profiles of coexisting thin and thick prewetting films are shown in Fig. 3(c), where we observe that the thick-film profile has a plateau near ρ_{liq}, and that $\rho(y) \to \rho_b$ as $y \to \infty$ for both profiles. Noteworthy is that the value of the density at contact with the wall, $\rho(0^+)$, is related to ρ_b via a sum rule (see Appendix B), which is exact for the given grand free energy functional, and thus can be used to further verify the numerics. We found the agreement of the calculation and the sum rule to be of the order of 10^{-7}.

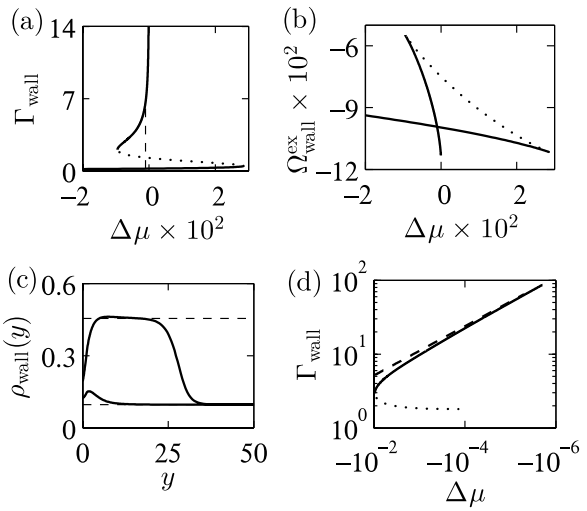

FIG. 3. Planar prewetting at $T = 0.92$, $\Delta\mu_{pw} = -0.1 \times 10^{-2}$. (a) and (b): $\Gamma_{wall}(\mu)$ and $\Omega^{ex}_{wall}(\mu)$ isotherms. Solid (dotted) branches are stable (unstable). The dashed vertical line in (a) is drawn at $\Delta\mu_{pw}$, where the branches in (b) intersect. (c) Density profiles of prewetting films. The dashed horizontal lines are at $\rho_{vap} \approx 0.096$ and $\rho_{liq} \approx 0.455$. (d) $\Gamma_{wall}(\mu)$ on a log-log plot for $\Delta\mu \to 0^-$. The dashed line shows the theoretical asymptote.

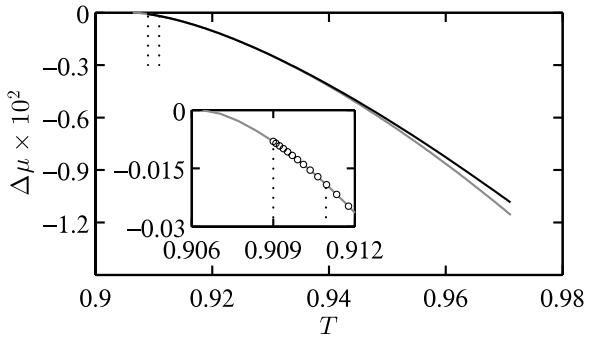

FIG. 4. Prewetting line of the planar wall, comparing our calculation (black curve), and the asymptotic fit (gray curve) used to extrapolate to saturation. The inset zooms into the region near T_w. Dotted vertical lines are drawn at $T = 0.909$ and $T = 0.911$, and demarcate the interval where 150 data points were used for fitting. The open circles show a selection of the data. The last data point is at $T \approx 0.9090$ and $\Delta\mu \approx 8 \times 10^{-5}$. Extrapolating to saturation gives $T_w \approx 0.9064$.

Figure 3(d) illustrates the divergence of $\Gamma_{wall}(\mu)$ as $\mu \to \mu_{sat}$ by plotting it on logarithmic axes. According to Eqs. (19) and (20), near saturation $\Gamma_{wall} \sim -a\Delta\mu^{-1/3}$, where the amplitude $a \approx (2A_H)^{1/3}\Delta\rho \approx 1.11$ for our value of T. This theoretical asymptote is plotted in Fig. 3(d) with a dashed line and shows an excellent agreement between the theory and the computation.

Figure 4 shows the calculated prewetting line $\Delta\mu_{pw}(T)$, where we observe that wall prewetting approaches saturation tangentially at T_w. This is to be expected, since by rewriting the Clausius–Clapeyron Eq. (23) with the help of surface excess quantities, one gets[47]

$$d\Delta\mu_{pw}/dT \sim -C/\Gamma_{wall}(\mu_{pw}), \text{ as } \mu_{pw} \to \mu_{sat}, \tag{32}$$

where $C > 0$ does not depend on μ, and $\Gamma_{wall}(\mu_{pw})$ corresponds to the thick coexisting film, whose height diverges as $T \to T_w$, so that $d\Delta\mu/dT \to 0$. Integrating Eq. (32) and using Eqs. (20) and (31), we obtain[15,47]

$$\mu_{sat} - \mu_{pw} \propto (T - T_w)^{3/2}, \tag{33}$$

which holds for LJ intermolecular interactions.

Since as $T \to T_w$, the liquid-vapor interface of the thick coexisting film unbinds to infinity, whereas the calculation of the density profiles is restricted to a finite domain, the calculation has to be terminated at some $T \gtrsim T_w$, and the last data point can be taken as an approximation to T_w (see inset of Fig. 4). One can also fit the power law $\Delta\mu_{pw} = a(T - T_w)^{3/2}$ through the data points near saturation and use it to extrapolate to $\Delta\mu = 0$ in order to obtain a better numerical value of T_w. We have used a total of 150 data points in the small interval within the vertical dotted lines in Fig. 4 to obtain the asymptote (gray curve).[48] We found $a \approx -0.8$ and a value for T_w within about 3% of the last computed value of T.

B. Slit pore

The Kelvin equation in (3) provides a simple approximation for the condensation transition, μ_c, in a slit pore. Using DFT, we can obtain the values of the surface tensions $\sigma_{lv}(T)$ and contact angles $\Theta(T)$ entering the Kelvin equation.

Alternatively, we can also directly obtain $\mu_c(T)$ by solving Eq. (22) as T varies. This direct approach captures fully the microscopic interactions, and the result should be different from the Kelvin prediction at high T.[18] It is certainly of interest to contrast the two at intermediate values of T.

To obtain the wall-fluid surface tensions, we solve Eq. (14) with $V_{\text{ext}}(\mathbf{r}) \equiv V_{\text{wall}}(y)$ and $\mu = \mu_{\text{sat}}$ for the density profiles $\rho_{\text{liq}}(y)$ and $\rho_{\text{vap}}(y)$ of the saturated liquid and vapor in contact with the planar wall. The boundary conditions are $\rho_{\text{liq}}(y) \to \rho_{\text{liq}}$ and $\rho_{\text{vap}}(y) \to \rho_{\text{vap}}$, as $y \to +\infty$, respectively. The wall-vapor and wall-liquid surface tensions (σ_{wv} and σ_{wl}) are given by their corresponding values of $\Omega^{\text{ex}}_{\text{wall}}(\mu_{\text{sat}})/A$, see Eq. (24). The liquid-vapor surface tension, σ_{lv}, is obtained in the same way, by setting $V_{\text{ext}}(\mathbf{r}) \equiv 0$ and solving Eq. (14) for the density profile of the free liquid-vapor interface. The boundary conditions are $\rho(y) \to \rho_{\text{vap}}$ and $\rho(y) \to \rho_{\text{liq}}$, as $y \to \pm\infty$.

From the surface tensions, we then compute the contact angle $\Theta(T)$ using Eq. (1), finding also that $T_s \approx 0.707$ by solving $\Theta(T_s) = \pi/2$ graphically. According to the Kelvin equation, the condensation curve should cross saturation at T_s and have a minimum near T_w (see Sec. I).

Figure 5 shows the condensation curves of two slit pores of widths $H = 40$ (black) and $H = 20$ (gray). The full and the dashed curves correspond to $\mu_c(T)$ obtained from Eqs. (22) and (3), respectively. For the Kelvin approximation, we have restricted the range of temperatures between T_s and $T = 0.97$ to keep the plot simple. Evidently, the wider pore is described well by the Kelvin equation at lower temperatures [$\Delta\mu_c(T_s) \approx 4 \times 10^{-4}$]. For higher T, the agreement breaks down. In the case of the narrower pore, the microscopic interactions neglected in the Kelvin equation noticeably affect condensation, for both high and low T [$\Delta\mu_c(T_s) \approx 3 \times 10^{-3}$]. For both slit pores, the Kelvin equation predicts a minimum near T_w, as expected. However, the DFT treatment shows the presence of the minimum for the wider pore, but not for the narrower pore, which can be attributed to the stronger fluid-substrate interactions with the second wall. Note also that unlike the Kelvin equation, DFT is capable of capturing the shift of the bulk critical point in slit pores.[18]

Figure 6 depicts the isotherms of adsorption (a) and excess grand potential (b) of the pore with $H = 40$ at T_s. The black and gray segments correspond to concave (stable and metastable) and non-concave (unstable) branches of $\Omega^{\text{ex}}_{\text{slit}}(\Delta\mu)$,

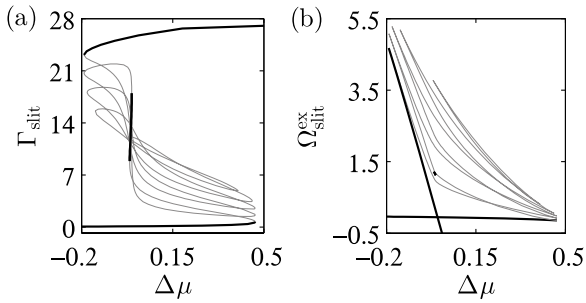

FIG. 6. Isotherms at $T_s \approx 0.707$ of adsorption (a) and excess grand potential (b) in a slit pore of width $H = 40$. Black: concave branches corresponding to stable vapor and capillary liquid and metastable film. Gray: non-concave branches. The metastable branch exists for $0.007 \lesssim \mu \lesssim 0.014$.

respectively. The value of T_s is quite low, and we find multiple solutions of Eq. (14), most of which are unstable. The unstable character of these states can be readily confirmed by going beyond the equilibrium theory and considering the dynamics of the system.[8,35,49–51]

We also note the existence of a metastable film adsorbed on the walls of the pore. The interval of $\Delta\mu$ where we find the film phase is rather narrow and has a width $\Delta_\mu \approx 7.6 \times 10^{-3}$. The metastable equilibria form a hardly noticeable concave branch on the $\Omega^{\text{ex}}_{\text{wall}}(\Delta\mu)$ isotherm, but span a large interval in adsorption, $\Delta_\Gamma \approx 9.1$. Figure 7 depicts the density profiles of vapor and capillary liquid (black) coexisting at T_s and $\Delta\mu_c(T_s) \approx 4 \times 10^{-4}$, and a representative profile of a metastable adsorbed film (dashed) at $\Delta\mu \approx 7.9 \times 10^{-3}$. Note the plateaus at ρ^c_{vap} and ρ^c_{liq}, which can be obtained as roots of Eq. (15) at $\mu = \mu_c$. In the example presented in Fig. 7, $\mu_c \gtrsim \mu_{\text{sat}}$, and we find that both $\rho^c_{\text{vap}} - \rho_{\text{vap}}$ and $\rho^c_{\text{liq}} - \rho_{\text{liq}}$ are positive and of $O(10^{-4})$, so capillary liquid is almost as dense as bulk liquid. Increasing H will isolate the walls more from each other, and part of the thin film branch will eventually become stable. In that case, there will be prewetting on the side walls of the pore at higher T.

C. Capped capillary

Consider now a capped capillary connected to the reservoir filled with vapor at T and μ [sketch in Fig. 1(c)]. To find the fluid density profile $\rho_{\text{cpd}}(x, y)$, we set $V_{\text{ext}}(\mathbf{r}) \equiv V_{\text{cpd}}(x, y)$ in

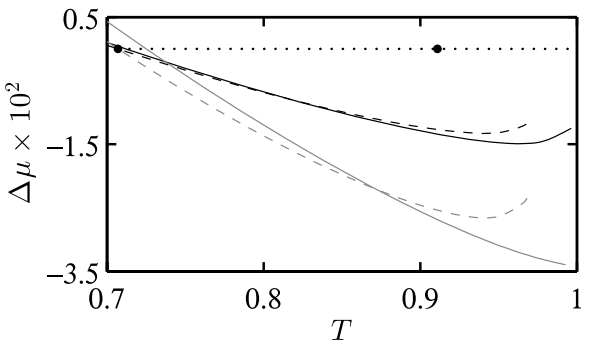

FIG. 5. Condensation curves of slit pores with $H = 20$ (gray) and $H = 40$ (black). DFT calculations (solid) and their respective Kelvin approximations (dashed). Dotted horizontal line shows $\Delta\mu = 0$. The leftmost and the rightmost solid circles mark T_s and T_w.

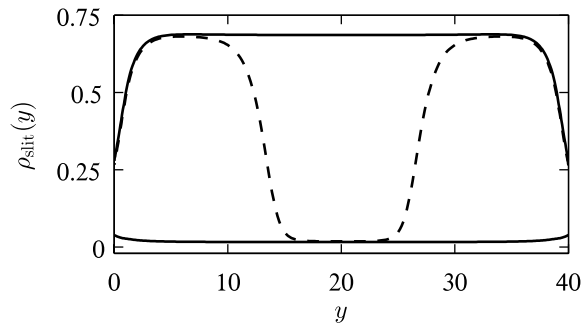

FIG. 7. Solid curve: profiles of vapor and capillary liquid coexisting during condensation at $T_s \approx 0.707$. Dashed curve: representative density profile of metastable film at $\Delta\mu \approx 7.9 \times 10^{-3}$, $\Gamma_{\text{slit}} \approx 16.2$. All profiles have plateaus of near-constant density at $\rho^c_{\text{vap}} \approx 0.02$ and $\rho^c_{\text{liq}} \approx 0.68$.

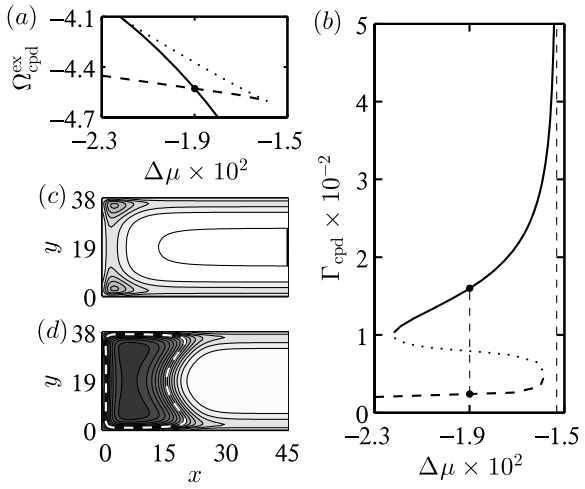

FIG. 8. Prewetting transition in a capillary with $H = 38$ at $T = 0.94$, where $\Delta\mu_{cpw}(T) \approx 1.9 \times 10^{-2}$ and condensation is continuous at $\Delta\mu_c(T) \approx -1.5 \times 10^{-2}$. (a) $\Omega^{ex}_{cpd}(\mu)$ isotherm. Full and dotted branches correspond to stable and unstable fluid states, respectively [same in (b)]. Two stable branches intersect at $\Delta\mu_{cpw}$. (b) $\Gamma_{cpd}(\mu)$ isotherm. The dashed vertical lines at $\Delta\mu_{cpw}$ and $\Delta\mu_c$ show the equal-area construction and the asymptote for $\Gamma_{cpd}(\mu)$, as $\mu \to \mu_c$, respectively. (c) and (d) Coexisting density profiles. The dashed white curve shows the position of the sharp interface.

Eq. (14), with $\rho_{cpd}(x,y) \to \rho_{slit}(y)$, as $x \to \infty$. The isotherms shown in Figs. 8(a) and 8(b) demonstrate the presence of a first-order transition at $\mu_{cpw} < \mu_c$, where vapor coexists with the capillary liquid slab adsorbed on the capping wall. We refer to this transition as capillary prewetting, by analogy with the transition observed for planar walls.[20]

The density profiles of coexisting fluid configurations are shown in Figs. 8(c) and 8(d), on a gray scale between $\rho^c_{vap} \approx 0.11$ (white) and $\rho^c_{liq} \approx 0.41$ (dark gray), with the sharp interface (dashed curve) defined along the contour of $(\rho^c_{vap} + \rho^c_{liq})/2$. As $\mu \to \mu_c$, the capillary liquid slab adsorbed on the capping wall [Fig. 8(d)] grows and completely fills the capillary. According to Eq. (29), the divergence of $\Gamma_{cpd}(\mu)$, as $\mu \to \mu_c$ indicates that the non-analyticity of $\Omega(\mu_c)$ corresponds to a continuous transition.

Equation (21) provides us with the asymptote $\Gamma_{cpd} \sim (\mu_c - \mu)^{-1/4}$, as $\mu \to \mu_c$. To compare it with the DFT calculation, we have selected three adsorption isotherms exhibiting continuous condensation corresponding to different values of H and T. Fitting the dependence $\Gamma_{cpd} = a(b-\mu)^q$ gives $a, b \approx \mu_c$ and $q \approx -1/4$. Figure 9 summarises our results and illustrates the divergence of Γ_{cpd} at condensation. In all calculations presented, the critical exponent is captured to within 1% of the theoretical value. In addition, the values μ_c obtained from fitting also agree within 1% with the condensation curves of the corresponding slit pores.

The locus of capillary prewetting transitions in the T-μ plane forms the curve $\mu_{cpw}(T)$. The height of coexisting slab grows as T is decreased along the capillary prewetting curve. Using Clausius–Clapeyron Eq. (23), we obtain

$$\frac{d(\mu_c - \mu_{cpw})}{dT} \sim \frac{C}{\Gamma_{cpd}(\mu_{cpw})} \quad \text{as} \quad \mu_{cpw} \to \mu_c, \tag{34}$$

where $C > 0$ does not depend on μ, and $\Gamma_{cpd}(\mu_{cpw})$ corresponds to the adsorbed capillary liquid slab. The relation above

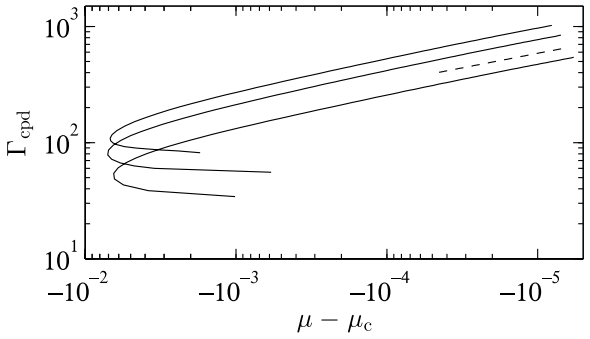

FIG. 9. Adsorption isotherms near respective μ_c. Dashed line: guide to the eye plotted according to $\Gamma_{cpd} \propto (\mu_c - \mu)^{-1/4}$. H and T for each isotherm from bottom to top (in parentheses, we provide the parameters obtained from fitting the power law $\Gamma_{cpd} = a(b-\mu)^q$ to the data, where b is used to calculate $\Delta\mu_c$): $H = 20$, $T = 0.91$ ($\Delta\mu_c \approx -2.67 \times 10^{-2}$, $q \approx -0.2509$, $a \approx 26.3$); $H = 30$, $T = 0.92$ ($\Delta\mu_c \approx -1.85 \times 10^{-2}$, $q \approx -0.2505$, $a \approx 43.0$); $H = 40$, $T = 0.94$ ($\Delta\mu_c \approx -1.45 \times 10^{-2}$, $q \approx -0.249$, $a \approx 55.0$).

is equivalent to $d\mu_c/dT \to d\mu_{cpw}/dT$, as $\mu_{cpw} \to \mu_c$, so that the curve $\mu_{cpw}(T)$ approaches the curve $\mu_c(T)$ tangentially as $T \to T_{cw}$, the capillary wetting temperature. Using the asymptote from Eq. (21), and integrating the slope in Eq. (34), we can also obtain the asymptote of the capillary prewetting curve in the case of LJ intermolecular potentials

$$\mu_c - \mu_{cpw} \propto (T - T_{cw})^{4/3} \quad \text{as} \quad T \to T_{cw}. \tag{35}$$

For $T < T_{cw}$, configurations with capillary liquid slabs are metastable and condensation is first-order. Conversely, for $T > T_{cw}$, capillary liquid slabs of finite height are stable when $\mu > \mu_{cpw}(T)$ and condensation is continuous. It then proceeds via the unbinding of the interface between capillary-liquid and vapour as $\mu \to \mu_c^-$. The temperature T_{cw} can be computed by finding the temperature for which the capillary prewetting curve $\mu_{cpw}(T)$ and the condensation curve $\mu_c(T)$ meet. Figure 10 shows several condensation (gray) and capillary prewetting (black) curves calculated for capillaries of different widths. In agreement with Eq. (34), each prewetting curve approaches the respective condensation curve tangentially. By recalling the earlier discussion on slit pores, we note the gradual disappearance of the local minima of the condensation

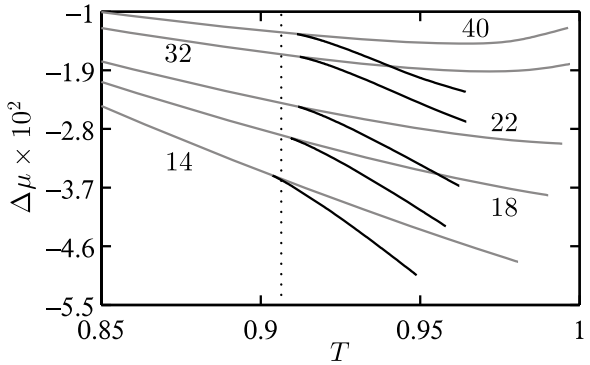

FIG. 10. Condensation (gray) and prewetting (black) lines of capped capillaries with different widths, H (top to bottom, also labelled in the plot): 40, 32, 22, 18, 14. The vertical dotted line marks the planar wetting temperature at $T_w \approx 0.906$.

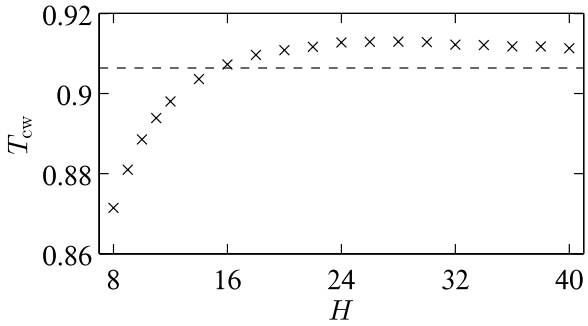

FIG. 11. Capillary wetting temperature as a function of capillary width (symbols). The dashed horizontal line marks T_w.

curves near T_w with the decrease of H and the gradual decrease of the critical condensation temperatures.

Figure 11 shows the width dependence of T_{cw}. For H between 8 and 12, the computations were performed in increments of 1 and for H between 12 and 40, in increments of 2. Calculating T_{cw} becomes more challenging as H is increased, because more mesh points are required to resolve the unbinding meniscus of the coexisting capillary liquid slabs. In the computations presented, we were able to resolve coexisting capillary liquid slabs of up to about 90 molecular diameters in length. For the values of H considered, such coexisting slabs correspond to temperatures $T > T_{cw}$, such that $\mu_c(T) - \mu_{pw}(T) \lesssim 10^{-4}$. These values of T are taken as reasonable approximations to T_{cw} in Fig. 11, since, according to Eq. (35), we expect these values to be within 0.1% of T_{cw}.

We see from Fig. 11 that for small values of H, $T_{cw}(H)$ is significantly lower than T_w. As H is increased, $T_{cw}(H)$ also increases, reaching a maximum between $H = 20$ and $H = 30$. As $H \to \infty$, it appears that $T_{cw} \to T_w^+$, which is to be expected physically, because the capillary prewetting line should tend to the planar prewetting line of the capping wall in this limit. For the values of H considered, we find that $|T_{cw} - T_w| \sim 6 \times 10^{-3}$ on average when $H > 20$. Thus, the planar wetting temperature provides a good estimate of the capillary wetting temperatures of mesoscopically wide pores. This result is in agreement with previous studies.[22,35]

IV. CONCLUDING REMARKS

In the present study, we have systematically investigated adsorption in planar walls, slit pores, and capped capillaries within the framework of classical DFT for fluids. The use of DFT is a compelling alternative approach to full-scale simulations, due to its ability to capture the main features of the phenomenology of complex fluid systems at small scales at a significantly lower computational cost.

For the purpose of computational efficiency, the underlying free-energy functional was kept as simple as possible. The adopted simplification is generally applicable for most single-component atomic fluids above the bulk triple point, where a functional with the local treatment of excluded volume interactions and the random phase approximation for long-range attractions provides an adequate description of wetting by a liquid-like fluid phase (such functionals would be inappropriate for studying other phenomena, such as, for example, layering or freezing).[23,27,28] Yet, our DFT approach is sufficiently sophisticated in that it ensures that the important interactions are retained.

With the help of continuation techniques, we have constructed complete phase diagrams with respect to μ and T, noting that in the same manner, one can relax other parameters in the system, such as those of the interaction potentials or the substrate geometry. Through continuation, we are also able to uncover all solutions to the Euler–Lagrange equation and eliminate the unstable ones by analyzing the convexity of the corresponding branches of the grand potential $\Omega(\mu)$. For a deeper understanding of the stability of the various fluid states obtained here, one makes use of dynamic DFT approaches, such as those developed recently by Goddard *et al.*[8,50]

Throughout this work, we emphasized that a comprehensive understanding of wetting in a capped capillary is facilitated by identifying links and common features with wetting in a slit pore and on a planar wall. In capped capillaries, condensation follows either the route of condensation in the associated slit pore (first-order transition, for $T \leq T_{cw}$) or a route similar to complete wall wetting (continuous transition, for $T > T_{cw}$). In the latter case, the fluid density profiles below condensation can develop mesoscopic plateaus corresponding to the denser capillary liquid phase, which is metastable far from the capping wall. The capillary prewetting curve, which joins the condensation curve tangentially at T_{cw}, demarcates the region of stability of capillary liquid slabs.

It is instructive to obtain an estimate of the wetting temperature of a capped capillary. First-order wetting transitions have been first predicted by Ebner and Saam,[54] and as an example, we take their model of interactions for argon ($\varepsilon/k_B = 119.76$ K, $\sigma = 3.405$ Å) in contact with solid CO_2 ($\varepsilon_w/k_B = 153.0$ K, $\sigma_w = 3.727$ Å, $\rho_w \sigma_w^3 = 0.988$). Choosing the coating parameter $H_0 = (\sigma_w + \sigma)/2$, we obtain $T_w \approx 105.3 \pm 0.1$ K. Hence, condensation in capped capillaries which are wider than 70 nm, should be first-order below 105 K, and continuous above that value. In narrower pores, the boundary between first-order and continuous condensation should be at even lower temperatures. It is important to emphasize that the value of T_w provided is merely an estimate and a more sophisticated free energy functional might be required to obtain a more accurate result.

Although continuous condensation is quite similar to complete wall wetting, and, as we have seen, T_w of the capping wall provides a reliable approximation to T_{cw}, there are important differences in the physics of the two systems. The adsorption of a mesoscopic liquid film on the planar wall below bulk saturation is due to the interactions of the fluid particles with the half-space filled by the substrate, whereas the adsorption of capillary liquid on the capillary capping wall below condensation is caused by the interactions between the fluid particles and the substrate slab "plugging" the slit pore. The fact that such slab is finite along the y-axis leads to different values of the critical exponents. The fluctuations of the fluid density along the z-axis, which are neglected in our DFT treatment, should play a more important role in the case of the capped capillary, than in the case of a planar wall.[15,46]

In the present work, we focused on capillaries with nanoscale widths, where the effects of wetting in the capillary

corners do not contribute to the wetting of the capped capillary below condensation. In wider pores, where the corners are sufficiently isolated, additional effects may take place below the condensation transition, such as the adsorption of drops in the capillary corners (so-called wedge prefilling transition).[46,52] For the nano-sized capillaries, we considered here, the corner drops remain metastable, as the relatively short distance between the side walls makes the formation of a single meniscus (that of the capillary liquid slab) more energetically efficient than the formation of two menisci (those of the corner drops). This may change, however, for rather wide pores, where the volume contributions of the adsorbate to the fluid free energy will dominate the surface contributions due to the interfaces. The system will then minimize the amount of the adsorbed liquid, rather than the surface area of the liquid-gas interfaces. As a result, two corner drops having a smaller total amount of adsorbate may be more energetically favored than a single capillary liquid slab in a range of chemical potentials below condensation. For wider pores, there may also exist a triple-point regime, where the drops in the corners coexist with a capillary-liquid slab (at least within a classical DFT treatment).

By analogy to continuous condensation, prewetting occurring at the side walls of a capped capillary is expected to be a continuous transition, manifested by the unbinding interfaces between the thin and thick prewetting films, where the latter are nucleated at the capping wall and are metastable far from it.[15,52] We shall consider this and related questions (e.g., the interplay between condensation in capped capillaries and wedge prefilling) in future studies.

ACKNOWLEDGMENTS

We acknowledge financial support from the European Research Council via Advanced Grant No. 247031 and the European Union-FP7 ITN Grant No. 214919 (Multiflow). We are grateful to the anonymous referees for valuable comments and suggestions and also to Professor Bob Evans and Professor Andy Parry for numerous stimulating discussions.

APPENDIX A: EXPRESSIONS FOR POTENTIALS

All expressions below are dimensionless and correspond to the parameters of Eq. (8) being set as units of length ($\sigma = 1$) and energy ($\varepsilon = 1$). If a fluid is brought in contact with a planar wall or a slit pore [1D problems, see Figs. 1(a) and 1(b)], its one-body density is a single-variable field, while in the capped capillary [2D problem, see Fig. 1(c)], it depends on two variables. The distribution $\rho(\mathbf{r})$ is obtained from Eq. (14). For one-dimensional problems, we have $\mathbf{r} \equiv y\mathbf{e}_\mathbf{y}$ ($r = y$), and

$$\rho(\mathbf{r}) \equiv \rho_{\text{wall}}(y) \text{ or } \rho(\mathbf{r}) \equiv \rho_{\text{slit}}(y), \tag{A1a}$$

$$V_{\text{ext}}(\mathbf{r}) \equiv V_{\text{wall}}(y) \text{ or } V_{\text{ext}}(\mathbf{r}) \equiv V_{\text{slit}}(y). \tag{A1b}$$

The expressions for the fluid-substrate potentials of the wall and the slit pore are given by Eqs. (10) and (11). Due to the fluid density being constant along the x- and z-axes, the expression in Eq. (8) can be simplified for one-dimensional problems, i.e., $\varphi_{\text{attr}}(y) \equiv \int_{-\infty}^{+\infty} dz \int_{-\infty}^{+\infty} dx\, \varphi_{\text{attr}}\left(\sqrt{x^2+y^2+z^2}\right)$,

$$\varphi_{\text{attr}}(y) = \begin{cases} -\dfrac{6\pi}{5}, & \text{if } |y| \le 1, \\ 4\pi\left(\dfrac{1}{5y^{10}} - \dfrac{1}{2y^4}\right), & \text{if } |y| > 1. \end{cases} \tag{A2}$$

In the two-dimensional problem, we have in Eq. (14), $\mathbf{r} \equiv x\mathbf{e}_\mathbf{x} + y\mathbf{e}_\mathbf{y}$ ($r = \sqrt{x^2+y^2}$), and

$$\rho(\mathbf{r}) \equiv \rho_{\text{cpd}}(x,y), \quad V_{\text{ext}}(\mathbf{r}) \equiv V_{\text{cpd}}(x,y), \tag{A3}$$

where the expression for the external potentials is defined in Eqs. (12) and (13). We compute the integral in Eq. (13) numerically using a highly accurate Clenshaw–Curtis quadrature and a spectral discretisation in 2D, which generalizes an earlier approach by Yatsyshin *et al.* in Ref. 35. Due to the fluid density being constant along the z-axis, the expression in Eq. (8) is simplified, i.e., $\varphi_{\text{attr}}(r) \equiv \int_{-\infty}^{+\infty} dz\, \varphi_{\text{attr}}\left(\sqrt{x^2+y^2+z^2}\right)$,

$$\varphi_{\text{attr}}(x,y) = \begin{cases} 2\displaystyle\int_{\sqrt{1-r^2}}^{\infty} dz\, \varphi_{1,1}^{6-12}\left(\sqrt{r^2+z^2}\right), & \text{if } r \le 1, \\ \dfrac{3\pi}{2}\left[-\left(\dfrac{1}{r}\right)^5 + \dfrac{21}{32}\left(\dfrac{1}{r}\right)^{11}\right], & \text{if } r > 1. \end{cases} \tag{A4}$$

Although the integral in the expression above can be given in closed form for $r \le 1$, see, e.g., the Appendix in the study by Pereira and Kalliadasis,[53] it is evaluated here by numerical quadrature since computations with the exact expression are prone to large round-off errors. In the region $r > 1$, we used the analytic expression given above.

APPENDIX B: PLANAR CONTACT THEOREM FOR LOCAL HARD SPHERE FUNCTIONALS

Here, we consider a LJ fluid in contact with a hard planar wall, see, e.g., the top panel of Fig. 1(a). The density $\rho(\mathbf{r}) \equiv \rho(y)$ satisfies Eq. (14) with $V_{\text{ext}}(\mathbf{r})$ being zero at $y > 0$ and infinite at $y \le 0$. Using the system of units explained at the beginning of Sec. III, we derive an analytic expression connecting the value of the density at contact with the wall, $\rho(0^+)$, with the bulk density ρ_b, where $\rho(y) \to \rho_\text{b}$, as $y \to +\infty$. The derivation for the cases of non-local hard sphere functionals can be found, e.g., in Refs. 23 and 27. The Euler-Lagrange Eq. (14) takes the form

$$\left.\frac{\delta f_{\text{HS}}^{\text{ex}}(\rho)}{\delta\rho(y_1)}\right|_{y_1=y} + \int_0^\infty dy_1 \varphi_{\text{attr}}(y-y_1)\rho(y_1) + T\ln\rho(y) - \mu = 0, \tag{B1}$$

where $f_{\text{HS}}^{\text{ex}}(\rho) \equiv \rho\psi(\rho)$ is the excess-over-ideal free energy density of the hard sphere fluid and $\varphi_{\text{attr}}(y)$ is given in Eq. (A2). The first term on the left-hand side of Eq. (B1) denotes the functional derivative of $\rho(y)\psi(\rho(y))$ with respect to $\rho(y)$, evaluated at y. We assume the existence of y_b, such that for $y \ge y_\text{b}$, the deviation of $\rho(y)$ from ρ_b is negligible. We also assume the existence of y_c, such that for $y \ge y_\text{c}$, the deviation of $\varphi_{\text{attr}}(y)$ from zero is negligible. To proceed, we take the derivative of Eq. (B1) with respect to y, then multiply the result by $\rho(y)$, and integrate from $y = 0^+$ to $y = y_\text{B} \equiv y_\text{b} + y_\text{c}$.

Applying integration by parts, as well as the thermodynamic relation between the pressure and the free energy, we arrive at the following expression connecting the density at contact and the bulk fluid pressure

$$P - P^{\mathrm{ex}}_{\mathrm{HS}}\left(\rho(0^+)\right) = T\rho(0^+), \tag{B2}$$

where $P^{\mathrm{ex}}_{\mathrm{HS}}(\rho)$ is the excess-over-ideal pressure of the hard sphere fluid,[25] see Eq. (16),

$$P^{\mathrm{ex}}_{\mathrm{HS}}(\rho) = \rho T \frac{1+\eta+\eta^2-\eta^3}{(1-\eta)^3} - \rho T. \tag{B3}$$

The generalization of the expression above to the case of an attractive wall, where $V_{\mathrm{ext}}(\mathbf{r}) \equiv V_{\mathrm{wall}}(y)$ and $\rho(\mathbf{r}) \equiv \rho_{\mathrm{wall}}(y)$ is straightforward: one needs to add the correction due to the component of the pressure tensor normal to the wall-fluid interface[27,34]

$$P - P^{\mathrm{ex}}_{\mathrm{HS}}\left(\rho_{\mathrm{wall}}(0^+)\right) + \int_0^{+\infty} dy\, \rho_{\mathrm{wall}}(y) \frac{dV_{\mathrm{wall}}(y)}{dy} = T\rho_{\mathrm{wall}}(0^+). \tag{B4}$$

The expressions in Eqs. (B2) and (B4) play the role of exact sum rules, which may be used as a further means to check our numerical implementation.

[1]M. Rauscher and S. Dietrich, Annu. Rev. Mater. Res. **38**, 143 (2008).
[2]K. Binder, Annu. Rev. Mater. Res. **38**, 123 (2008).
[3]S. Herminghaus, M. Brinkman, and R. Seeman, Annu. Rev. Mater. Res. **38**, 101 (2008).
[4]S. Mandal, S. Lang, M. Gross, M. Oettel, D. Raabe, T. Franosch, and F. Varnik, Nature **5**, 4435 (2014).
[5]E. Chiavazzo, M. Fasano, P. Asinari, and P. Decuzzi, Nat. Commun. **5**, 4565 (2014).
[6]Z. Gou and W. Liu, Plant Sci. **172**, 1103 (2007).
[7]H. Craighead, Nature **442**, 387 (2006).
[8]B. D. Goddard, A. Nold, N. Savva, P. Yatsyshin, and S. Kalliadasis, J. Phys.: Condens. Matter **25**, 035101 (2013).
[9]J. Reinhardt, A. Scacchi, and J. M. Brader, J. Chem. Phys. **140**, 144901 (2014).
[10]J. Bleibel, A. Dominguez, M. Oettel, and S. Dietrich, Soft Matter **10**, 4091 (2014).
[11]I. Gerlach, M. Kawase, and K. Miura, Microporous Mesoporous Mater. **122**, 79 (2009).
[12]A. Calvo, B. Yameen, F. J. Williams, G. J. A. A. Soler-Illia, and O. Azzaroni, J. Am. Chem. Soc. **131**, 10866 (2009).
[13]M. Nosonvsky and B. Bhushan, Curr. Opin. Colloid Interface Sci. **14**, 270 (2009).
[14]A. Nikolov and D. Wasan, Eur. Phys. J.: Spec. Top. **197**, 325 (2011).
[15]W. F. Saam, J. Low Temp. Phys. **157**, 77 (2009).
[16]D. Bonn and D. Ross, Rep. Prog. Phys. **64**, 1085 (2001).
[17]M. Schick, in *Les Houches 1988. Liquids at Interfaces*, edited by J. Charvolin, J. F. Joanny, and J. Zinn-Justin (North-Holland, 1990), p. 415.
[18]S. Dietrich, in *Phase Transitions and Critical Phenomena*, edited by C. Domb and J. L. Lebowitz (Academic Press, 1988), p. 2.
[19]A. O. Parry, C. Rascon, N. B. Wilding, and R. Evans, Phys. Rev. Lett. **98**, 226101 (2007).
[20]P. Yatsyshin, N. Savva, and S. Kalliadasis, Phys. Rev. E **87**, 020402(R) (2013).
[21]A. Malijevský, J. Chem. Phys. **137**, 214704 (2012).
[22]C. Rascon, A. Parry, R. Nurnberg, A. Pozzato, M. Tormen, L. Bruschi, and G. Mistura, J. Phys.: Condens. Matter **25**, 192101 (2013).
[23]J. F. Lutsko, *Adv. Chem. Phys.* (John Wiley & Sons, 2010), p. 1.
[24]J. Hansen and I. McDonald, *Theory of Simple Liquids*, 3rd ed. (Elsevier, 2006).
[25]N. F. Carnahan and K. E. Starling, J. Chem. Phys. **51**, 635 (1969).
[26]J. A. Barker and D. Henderson, J. Chem. Phys. **47**, 4714 (1967).
[27]R. Roth, J. Phys.: Condens. Matter **22**, 063102 (2010).
[28]A. Nold, D. N. Sibley, B. D. Goddard, and S. Kalliadasis, Phys. Fluids **26**, 072001 (2014).
[29]D. E. Sullivan and M. M. Telo da Gama, in *Fluid Interfacial Phenomena*, edited by C. A. Croxton (Wiley, New York, 1986), p. 45.
[30]P. Tarazona, U. M. B. Marconi, and R. Evans, Mol. Phys. **60**, 573 (1987).
[31]R. Evans, in *Les Houches 1988. Liquids at Interfaces*, edited by J. Charvolin, J. F. Joanny, and J. Zinn-Justin (North-Holland, 1990), p. 1.
[32]A. Chizmeshya, M. W. Cole, and Z. Zaremba, J. Low Temp. Phys. **110**, 677 (1998).
[33]A. Nold, A. Malijevský, and S. Kalliadasis, Phys. Rev. E **84**, 021603 (2011).
[34]J. R. Henderson, in *Fundamentals of Inhomogeneous Fluids*, edited by D. Henderson (Marcel Dekker, New York, 1992), p. 23.
[35]P. Yatsyshin, N. Savva, and S. Kalliadasis, J. Chem. Phys. **136**, 124113 (2012).
[36]M. G. Knepley, D. A. Karpeev, S. Davidovits, R. S. Eisenberg, and D. Gillespie, J. Chem. Phys. **132**, 124101 (2010).
[37]L. J. D. Frink, A. G. Salinger, M. P. Sears, J. D. Weinhold, and A. L. Frischknecht, J. Phys.: Condens. Matter **14**, 12167 (2002).
[38]L. J. D. Frink and A. G. Salinger, J. Comput. Phys. **159**, 407 (2000).
[39]N. Savva and S. Kalliadasis, Phys. Fluids **21**, 092102 (2009).
[40]N. Savva and S. Kalliadasis, Europhys. Lett. **94**, 64004 (2011).
[41]J. P. Boyd, *Chebyshev and Fourier Spectral Methods* (Dover Publications, 2001).
[42]L. N. Trefethen, *Spectral Methods in MATLAB* (SIAM, 2000).
[43]N. Hale and L. N. Trefethen, SIAM J. Numer. Anal. **46**(2), 930 (2008).
[44]S. Dhawan, M. E. Reimel, L. E. Scriven, and H. T. Davis, J. Chem. Phys. **94**, 4479–4489 (1991).
[45]A. G. Salinger and L. J. D. Frink, J. Chem. Phys. **118**(16), 7457 (2003).
[46]K. Rejmer, S. Dietrich, and M. Napiorkowski, Phys. Rev. E **60**, 4027 (1999).
[47]E. H. Hauge and M. Schick, Phys. Rev. B **27**, 4288 (1983).
[48]J. C. Lagarias, J. A. Reeds, M. H. Wright, and P. E. Wright, SIAM J. Optim. **9**, 112 (1998).
[49]B. D. Goddard, G. A. Pavliotis, and S. Kalliadasis, Multiscale Model. Simul. **10**, 633 (2012).
[50]B. D. Goddard, A. Nold, N. Savva, G. A. Pavliotis, and S. Kalliadasis, Phys. Rev. Lett. **109**, 120603 (2012).
[51]B. D. Goddard, A. Nold, and S. Kalliadasis, J. Chem. Phys. **138**, 144904 (2013).
[52]E. H. Hauge, Phys. Rev. A **46**, 4994 (1992).
[53]A. Pereira and S. Kalliadasis, J. Fluid Mech. **692**, 53 (2012).
[54]C. Ebner and W. F. Saam, Phys. Rev. Lett. **38**, 1486 (1977).